Mechanical Deformations of a Liquid Crystal Elastomer at Director Angles Between 0° and 90°: Deducing an Empirical Model Encompassing Anisotropic Nonlinearity

Devesh Mistry [ORCID],[†] **Helen F. Gleeson** [ORCID]

School of Physics and Astronomy, University of Leeds, Leeds LS2 9JT, United Kingdom
Correspondence to: D. Mistry (E-mail: deveshmistry@outlook.com)

ABSTRACT: Despite the wealth of studies reporting mechanical properties of liquid crystal elastomers (LCEs), no theory can currently describe their complete mechanical anisotropy and nonlinearity. Here, we present the first comprehensive study of mechanical anisotropy in an all-acrylate LCE via tensile tests that simultaneously track liquid crystal (LC) director rotation. We then use an empirical approach to gain a deeper insight into the LCE's mechanical responses at values of strain, up to 1.5, for initial director orientations between 0° and 90°. Using a method analogous to time–temperature superposition, we create master curves for the LCE's mechanical response and use these to deduce a model that accurately predicts the load curve of the LCE for stresses applied at angles between 15° and 70° relative to the initial LC director. This LCE has been shown to exhibit auxetic behavior for deformations perpendicular to the director. Interestingly, our empirical model predicts that the LCE will further demonstrate auxetic behavior when stressed at angles between 54° and 90° to the director. Our approach could be extended to any LCE; so it represents a significant step forward toward models that would aid the further development of LCE theory and the design and modeling of LCE-based technologies. © 2019 The Authors. *Journal of Polymer Science Part B: Polymer Physics* published by Wiley Periodicals, Inc. J. Polym. Sci., Part B: Polym. Phys. **2019**, *57*, 1367–1377

KEYWORDS: anisotropic elasticity; empirical model; liquid crystal elastomer; mechanical properties; nonlinear elasticity

INTRODUCTION A current trend in materials science is to develop soft materials, which can mimic the structure, anisotropy, and functionality of materials and tissues found in nature.[1–6] Developing such materials would enable and increase the functionality of next-generation technologies such as soft robotics and biomedical devices.[7–9] Liquid crystal elastomers (LCEs), which incorporate liquid crystal (LC) order into a lightly crosslinked polymer network, are one such class of bio-similar materials—celebrated for their unique mechanical behaviors and their remarkable shape responsivity.[4,10–21] While the majority of LCE research typically focuses on the development and application of their shape actuation behavior, there is an increasing body of research studying the use of LCEs as mechanical and structural materials in fields such as flexible electronics and biomedical devices.[22–25] In these fields, an LCE's mechanical anisotropy and programmability, shape programmability, and shock dissipation offer the prospect of bio-inspired devices with enhanced functionality and robustness over existing devices.

Currently, LCE devices are limited to laboratory prototypes, partly because the full structure–property relationships of LCEs are yet to be understood, and so real-world devices cannot yet be designed and developed. For instance, while much research has investigated the mechanical behaviors of the so-called monodomain LCEs (in which the average molecular orientation—or LC director—is aligned over macroscopic length scales), the vast majority of studies performed to date focus solely on the case of stresses applied perpendicular to the LC director.

When taken together, the few known experimental LCE studies that have considered stresses applied at angles other than 90° to the director clearly show that the general mechanical behavior of LCEs is highly complex and nonlinear. Specifically,

---

an LCE's load curve shape is fundamentally dependent on the initial director angle and how the director rotates with increasing strain.[15,22,26,27] However, the existing studies are limited by the fact most do not simultaneously report the load curve shape and the director rotation behavior for LCEs prepared with a range of initial director angles spanning between 0° and 90°. Therefore, the precise dependency of the relationship between load curve shape and LCE anisotropy remains unknown. Moreover, as LCE behaviors are strongly dependent on LCE chemistry, one cannot draw conclusions from pieces of data taken from multiple studies performed on different materials.[19,28–30] Put simply, almost 40 years, since the first LCE was synthesized by Finkelmann and coworkers, a complete picture of a single LCE anisotropic tensile mechanical behavior does not yet exist.

In this article, we address this knowledge gap by performing tensile mechanical tests of an all-acrylate, low-glass transition temperature LCE prepared in monodomain samples and stressed at a range of angles relative to the director. By simultaneously monitoring the stress and director orientation dependencies on applied strain, we build a comprehensive picture of the LCE mechanical anisotropy. We show that while aspects of neoclassical LCE theory by Warner and Terentjev appear to successfully describe some of the behaviors observed, a complete understanding that can predict the behavior of the LCE is only achieved through the development of an empirical model based on the superposition of tensile load curves via the recorded orientations. The model we develop is currently capable of accurately describing the tensile and director rotation behavior of the LCE when stressed at any intermediate initial angle between 15° and 70° to the director. We propose that our model could be used to aid the creation of finite element models of the LCE that would ultimately allow the simulation of LCE-based mechanical devices. Moreover, our study demonstrates a novel method for deducing empirical models of the mechanical anisotropy and nonlinearity LCEs—a method that perhaps could be extended to other anisotropic materials.

EXPERIMENTAL

The synthesis procedure of the LCE used here has been described in detail previously.[19] Briefly, the chemical components displayed in Figure 1 were mixed together in the composition indicated to form an LCE precursor with a nematic to isotropic transition temperature (T_{NI}) of 36 °C. 6-(4-Cyano-biphenyl-4′-yloxy)hexyl acrylate (A6OCB), 1,4-bis-[4-(6-acryloyloxyhex-yloxy)benzoyloxy]-2-methylbenzene (RM82), and 4′-hexyloxybiphenyl (6OCB) are low-molar mass liquid crystalline molecules. The nonreactive 6OCB is used to broaden the nematic phase range of the LCE precursor monomer mixture. A6OCB and 2-ethylhexyl acrylate polymerize to form polymer chains that are crosslinked via the RM82 groups. Photopolymerization of the LCE is initiated by methyl benzoylformate (MBF).

The precursor was capillary filled in the isotropic phase (at approximately 40 °C) into LC devices of dimensions 60 × 15 cm and of cell gap (z) of ~100 μm. The cell substrates
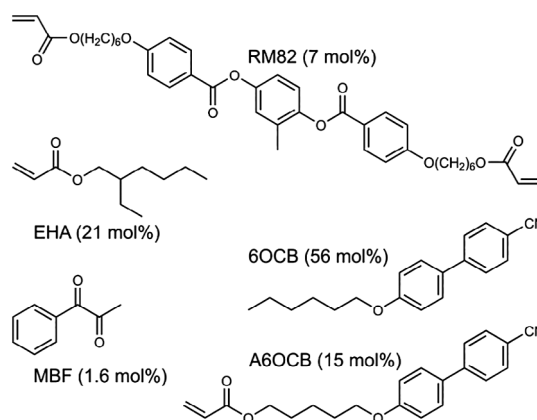

FIGURE 1 Structures of the chemicals, 6-(4-cyano-biphenyl-4′-yloxy)hexyl acrylate (A6OCB), 2-ethylhexyl acrylate (EHA), 1,4-bis-[4-(6-acryloyloxyhex-yloxy)benzoyloxy]-2-methylbenzene (RM82), 4′-hexyloxybiphenyl (6OCB), and methyl benzoylformate (MBF), used to produce the LCE under test. Figures shown in the brackets gives the percentage by mole, which gives the composition of the LCE precursor from which the LCE is polymerised.

were prepared with a uniaxially rubbed poly(vinyl alcohol) alignment layer. Upon filling, the cells were cooled to room temperature and left for half an hour for a monodomain nematic phase to form. The LCEs were then polymerised using a 2.5 mW cm^{-2} fluorescent UV light source for 2 h to ensure complete polymerization. The polymerised LCEs were then washed in methanol and dichloromethane to remove the 6OCB and any unreacted MBF and then hung to dry. Full details of how the LC devices were prepared and the LCE synthesized are given in ref. 19 and its Supporting Information.[19]

For mechanical testing, ~2 × 20 mm films of LCE were cut with the LC director at a variety of angles, θ_i, relative to the film long axis. The geometry and coordinate system used are illustrated in Figure 2. The accuracy with which we could cut samples with an intended director angle was typically ±2°. Thus, after cutting samples, the actual director angle for each sample was determined with an accuracy of ±1°.

Optomechanical testing of the LCE films was performed using bespoke equipment described in detail in ref. 19 and its Supporting Information.[19] Briefly, the equipment consists of a miniature tensile testing enclosure containing actuators and a load cell for measuring the stress–strain curve of a low-modulus material. During mechanical testing, the equipment allows for simultaneous observation of the sample between crossed polarizers via transmitted white light—enabling the localized deformations and LC director orientation to be deduced simultaneously.

During each test, the samples were extended in 0.5-mm steps until failure. After each extension step, the sample was allowed to stress relax for 2 min before 36 crossed polarizing photographs (polarizers rotated by 10° between photographs) and one transmitted white light photograph of the sample
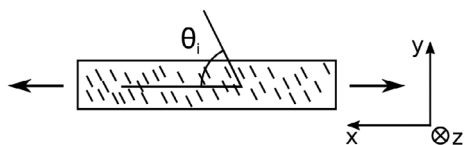
FIGURE 2 Illustration of sample geometries and coordinate set used. The director angles are measured with respect to the applied stress (*x*) axis.

were captured and a load cell reading taken. From the crossed polarizing photographs, the director angle at the center of the sample was deduced by finding the minimum of the transmitted light intensity.[19] From the white light photographs, the relative separation of sample features was tracked using a python package, trackpy, in order to deduce the localized strain at the center of the sample.[31] Together with the load cell readings, the localized strains allowed the tensile load curve of each sample to be deduced. This testing procedure is identical to that previously used in a fundamental mechanical characterization of the present LCE at director angles of 2° and 88°.[19]

As in this article, we aim to deduce how the strain-dependent LC director angle affects the shape of the LCE tensile load curve—regardless of strain, we consider the true stresses evolved within the tested LCE samples as opposed to the engineering stresses. We also calculate true initial modulus values using the derivative to true stress to total strain. In our use of true stresses and true moduli, there are key assumptions important to define.

To a first approximation, considering the true stresses removes the strain dependency of the tensile load curves. We have previously shown that when strained perpendicular to the director, the present LCE conforms well to the shear-free volume conserving condition of $\lambda_x \lambda_y \lambda_z = 1$ (where λ_i is the deformation along the *i*th principle axis)—even at strains of 150%.[16] While director rotations within the plane of deformation may give rise to shear contributions, λ_{xy} and λ_{yx}, these are neglected in this work for simplicity. Thus, in all cases, we calculate the true stress (which accounts for the strain-dependent sample cross-sectional area) by multiplying the engineering stress (force divided by initial sample cross-sectional area) by the longitudinal deformation, $\lambda_x = \epsilon_x + 1$, where ϵ_x is the longitudinal strain.[16,32]

In calculating elastic moduli from functions fitted to true stress load curves, we take the derivative with respect to the total strain. The total strain will, however, have two contributions—a component from the purely elastic deformation of the network (and hence LC order parameter)[19] and a spontaneous component from the rotation of the anisotropic polymer conformation/LC director. Therefore, there will essentially be two coupled elastic moduli. As in this work, we are concerned with the overall material behavior, and since we cannot currently determine the individual contributions to the total strain, we will use the true elastic modulus calculated via the derivative of true stress to overall strain.

RESULTS AND DISCUSSION

Load Curve Anisotropy and Initial Elastic Modulus

Figure 3 shows the true stress tensile load curves for the various samples of LCE prepared with a variety of different initial director angles (between 2° and 88°). As intuitively expected, these data show that the greater the angle between the initial director orientation and the applied stress, θ_i, the softer the elastic response and the greater the maximum sustainable strain before failure. The load curves shown here are broadly consistent with the behavior reported by Ware et al. for their main-chain, acrylate-amine LCE (engineering stress load curves of our LCE are shown for comparison in the Supporting Information Fig. S1). However, the Ware LCE load curves all show, to varying extents, step-like shapes where the load curves begin with a steep gradient (high modulus) which
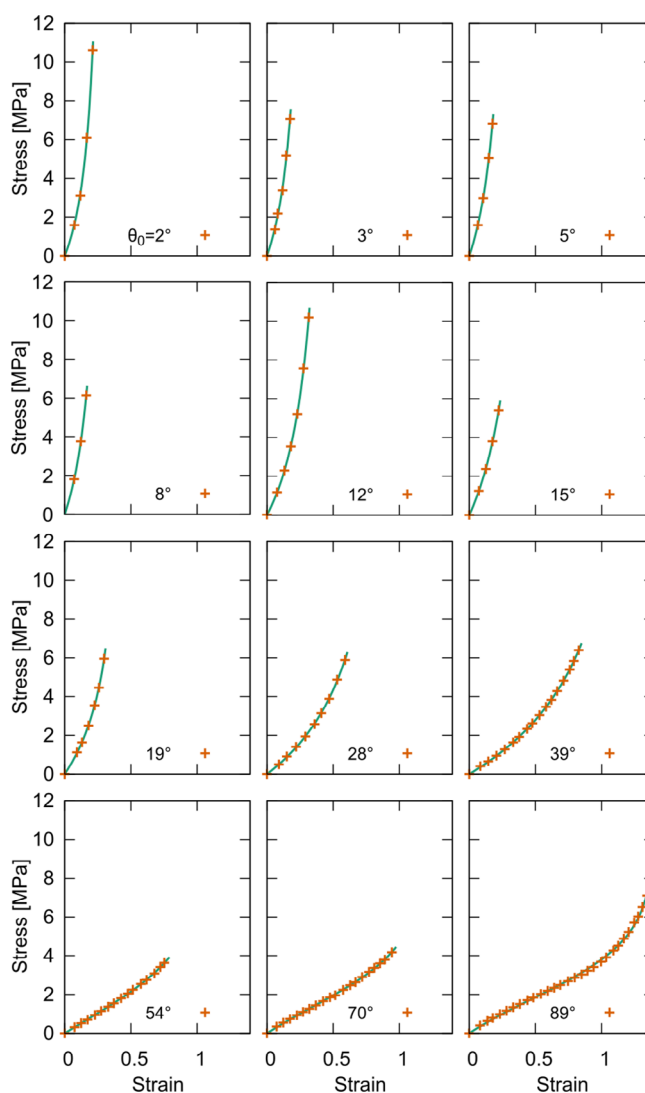

FIGURE 3 True stress load curves fitted with the inverse sigmoidal function (form given in eq 1). Fitted parameters are shown in Table 1. For $\theta_i = 2° - 8°$, there are notably few data points available for fitting. The uncertainties on the initial moduli given in Table 1 take this into account. [Color figure can be viewed at wileyonlinelibrary.com]

decreases until the load curve takes a linear form. By comparison for the present LCE, such "steps" in the load curves are only seen for the samples with θ_i of 54°, 70°, and 88°.

During mechanical testing, all samples with $\theta_i \geq 12°$ were seen to fail at the clamps. This could be explained by director rotation at the clamps causing stress concentrations toward one edge of the film, which in turn cause failure. Consequently, the failure point recorded for samples with $\theta_i \geq 12°$ may be premature failure points, and therefore, the maximum stresses recorded are underestimates of the actual maximum stresses sustainable for the central portion of each film.

To facilitate comparing and understanding the tensile mechanical response of the present LCE, we have fitted each of the load curves from Figure 3 with curve of the form

$$\sigma_T = A \times \log\left(\frac{1 + c\epsilon_x}{1 - d\epsilon_x}\right), \tag{1}$$

where σ_T is the true stress, ϵ_x is the applied strain, and A, c, and d are free parameters. Equation 1 is an inverse sigmoidal function constrained to pass through the origin (as a load curve must). An inverse sigmoidal functional form was a pragmatic choice of a function with minimal free parameters, and a correct shape for fitting to each load curve, for example, the 88° curve, has a sigmoidal-like "S" shape reflected in the line $y = x$. It is important to explicitly note that despite the quality of the fits of this single function to all of the load curves presented, to the best of our knowledge, there is no theoretical basis for our function choice.

The fitted parameters for each load curve are shown in Table 1. The last column of Table 1 shows values of the initial

elastic modulus for each load curve calculated from the derivative of eq 1.

$$E(\epsilon_x) = \frac{d\sigma_T}{d\epsilon_x} = \frac{A \times (c + d)}{(1 + c\epsilon_x)(1 - d\epsilon_x)}, \tag{2}$$

where $E(\epsilon_x)$ is the true modulus as a function of strain, ϵ_x. For determining the initial elastic modulus, ϵ_x is set to zero. For samples with $\theta_i \leq 54°$, the fits performed to the whole data accurately fit to the low-strain data points. Supporting Information Figure S2 (a) shows, as an example, a magnified view of the low-strain data and fit for the 54° sample. Supporting Information Figure S2(b,c) shows that by comparison, the fits of Figure 3 made to the 70° and 88° data miss the low-strain data points. Additional curves shown are fitted solely to the low-strain data points, from which more accurate values of the initial elastic modulus can be calculated. The row of Table 1 marked with footnote "a" shows the fitted parameters and calculated initial elastic moduli for the low-strain fits of the 70° and 88° data. While these data agree within error to those deduce from fits to the whole data sets, Supporting Information - Figure S2(a) clearly shows the low-strain fits give more accurate values for the elastic modulus for the 70° and 88° data.

Figure 4 shows the calculated elastic moduli plotted against θ_i. For the 70° and 88° samples, the moduli from fits to the low-strain data points are used. We can additionally fit the expected variation in initial modulus with angle for orthotropic materials (determined from the stiffness matrix of classical elasticity).[33,34]

$$\frac{1}{E_\theta} = \frac{\cos^4\theta}{E_1} + \frac{\sin^4\theta}{E_2} + \frac{\sin^2(2\theta)}{4k}, \tag{3}$$

TABLE 1 Parameters and Moduli from Fitting eq 1 to True Stress Load Curves (Fig. 2)

Initial Director Angle, θ_i (°)	Function Fitting Parameters			Initial Elastic Modulus (MPa)
	A	c	d	
2	182	−3.06	3.15	17 ± 2
3	138	−2.90	3.04	20 ± 2
5	135	−2.64	2.80	20 ± 2
8	78.8	−2.73	2.98	20 ± 2
12	80.5	−1.81	1.97	13 ± 1
15	41.6	−1.54	1.91	15 ± 1
19	4.23	−0.13	2.57	10 ± 1
28	6.86	−0.38	1.13	5.2 ± 0.7
39	5.48	−0.11	0.87	4.1 ± 0.6
54	1.95	1.23	0.93	4.2 ± 0.1
70	1.60	1.92	0.84	4.4 ± 0.7
70[a]	1.02	3.86	1.11	5.1 ± 0.2
88	1.59	2.14	0.71	4.5 ± 0.8
88[a]	1.34	3.20	0.73	5.3 ± 0.2

Errors on initial moduli were manually deduced assessing curves plotted against low-strain data.

[a] Fits performed to low-strain data points.

where

$$\frac{1}{k} = \frac{1}{G_{12}} - \frac{2\nu_{21}}{E_2}. \qquad (4)$$

In eqs 3 and 4, E_1 is the modulus along the principal axis (in this case, the x axis), E_2 is the modulus perpendicular to the principal axis, in this case, the modulus in the yz plane, G_{12} is the axial shear modulus in the 1–2 plane, and ν_{21} is the Poisson's ratio for a strain, ϵ_2, induced in response to an applied strain, ϵ_1. In fitting, E_2 was fixed at 5.3 MPa (Table 1) and E_1 and k were free parameters found to be 20 and 1.7 MPa, respectively. Since the form of eq 3 does not allow it to replicate the apparent initial increase in modulus between $\theta_i = 0°$ and $10°$, it is not surprising that the best-fitted value for E_1 lies outside the range (17 ± 2 MPa) measured from the $2°$ sample. As we have previously deduced that, for the present LCE, $\nu_{21} \cong 0$, the above fitting allows us to deduce an approximate value for G_{12} of 1.7 MPa.[16]

Figure 4 shows that the model described by eq 3 fits well to the experimentally measured data—almost passing through the error bars of all points. The model replicates the key features of the sharp decrease in modulus between $\theta_i = 10°$ and $30°$ and the modulus minimum occurring for $\theta_i < 90°$. However, the model does not replicate the apparent initial increase in modulus at low θ_i (discussed above) and the modulus minimum at $\theta_i = 45°$ (fourth order polynomial fitted to data gives the minimum to be at $\theta_i = 44.9°$). Indeed, the model can only exhibit a minimum at $\theta_i = 45°$ for $G_{12} \to 0$ at which point $E_\theta = 0$ for all angles.

Director Rotation Behavior

Figure 5 shows, for each of the tested samples, the evolution of the director orientation with imposed strain along with model
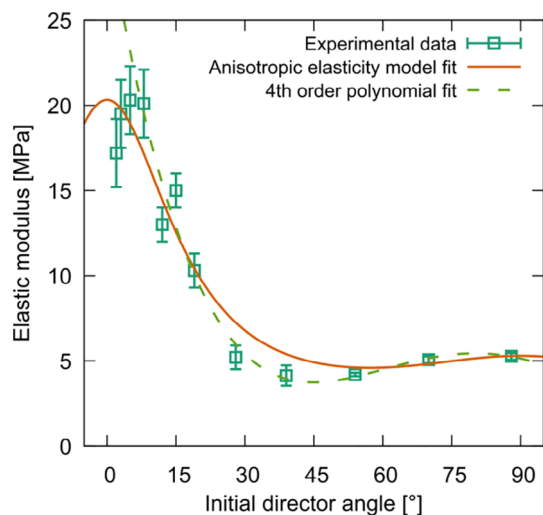

FIGURE 4 The initial elastic modulus of the studied LCE from Table 1. For the $\theta_i = 70°$ and $88°$ samples, moduli shown are from fits made to low-strain data. The fourth order polynomial fitted to the $\theta_i = 8 - 88°$ data has a minimum at $\theta_i = 44.9°$. [Color figure can be viewed at wileyonlinelibrary.com]
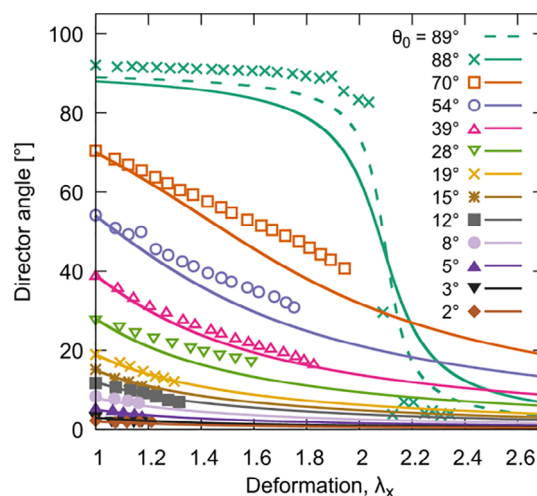

FIGURE 5 Director orientation curves plotted against the deformation, $\lambda_x = \epsilon_x + 1$, parallel to the stress axis. Points correspond to experimentally measured points. Calculated curves are generated using eq 3 and $\lambda_c = 2.1$. [Color figure can be viewed at wileyonlinelibrary.com]

curves of the expected director rotation behavior (described and discussed below). In all cases, the director rotates with strain toward the stress axis as would be expected. The forms of director rotation for the $\theta_i = 88°$ and $70°$ samples appear similar to those reported by Hirschmann et al. for their all-acrylate LCEs prepared with $\theta_i = 89°$ and $67°$.[27] This similarity in behavior is to be expected as, like the present LCE, the LCE studied by Hirschmann et al. (first reported by Mitchell et al.) deforms via a "Mechanical Fréedericksz Transition" (MFT) process when stressed perpendicular to the director as opposed to via semi-soft elasticity as is observed in other LCEs.[27,35]

In the previous section, we were able to fit all the load curve data quite accurately with a single function. Achieving a similar result for the strain dependence of the director orientation will allow us to relate the mechanical deformations for each curve to the strain-dependent director orientation. As Hirschmann et al. were able to well fit a model for director rotation developed by Bladon et al. in the MFT framework (with an assumed constant order parameter), we use the same model here.[27,36]

Bladon et al. derived the following equation for describing the director orientation, θ (relative to the stress axis), based on the initial director angle relative to the stress axis (θ_i) and the applied deformation, λ_x.[36]

$$\tan 2\theta = \frac{2 \times (\lambda_c^3 - 1) \times \lambda_x^{3/2} \times \sin(2\theta_0)}{(\lambda_c^3 + 1)(\lambda_x^3 - 1) + (\lambda_c^3 - 1)(\lambda_x^3 + 1) \times \cos(2\theta_0)}, \qquad (5)$$

where λ_c is the critical deformation for director reorientation in the MFT model.[36]

In Figure 5, we have plotted model curves using $\lambda_c = 2.1$ (as deduced from the $\theta_i = 88°$ curve) and values of θ_i corresponding to each experimental data set. We have also

plotted an additional model curve using $\theta_i = 89°$ (green dashed line) for comparison with the $\theta_i = 88°$ model and experimental data. We see that the model curve for $\theta_i = 89°$ lies much closer to the experimental data points than the model curve for $\theta_i = 88°$. This slight disagreement is not too surprising given the present LCE is known to have a strain-dependent order parameter when stretched perpendicular to the director, while eq 5 assumes a constant order parameter.[16,19]

Turning our attention to the rest of the data, we note that for samples prepared with director angles $\theta_i \gtrsim 30$, the model curves agree well with the experimental data at low strains; however, with increasing strain, the model tends to over-predict the magnitude of director rotation. For samples with $\theta_i \lesssim 30°$, the model curves agree very well with the experimental data for the full mechanical test. Overall, we would say the level of agreement between the model and experimental data is remarkably good given the model developed by Bladon et al. assumes a constant LC order parameter (and hence polymer conformation anisotropy) when we know this is not necessarily true for the present LCE.[16]

Analyzing eq 5 a little further allows us potential insight to why, in Figure 4, we saw that $\theta_i = 45°$ corresponds to the minimum in the initial elastic modulus. Differentiating eq 5 with respect to λ_x and considering the unstrained state, that is, $\lambda_x = 1$, gives the following result (see Supporting Information Section 1):

$$\therefore \frac{d\theta_i}{d\lambda_x} = -\frac{3(\lambda_c^3 + 1)}{4(\lambda_c^3 - 1)} \sin(2\theta_0), \qquad (6)$$

which has a minimum for $\theta_i = 45°$—that is, the director rotating toward the strain axis (thus decreasing) at its fastest. According to the theory of Warner and Terentjev, director rotation provides a mechanism for a spontaneous strain, allowing a reduction in the free energy cost of an LCE mechanical deformation and hence a reduction in the elastic modulus calculated using the overall strain. As the initial director rotation is at its greatest for $\theta_0 = 45°$, the spontaneous strain will also be at its greatest for $\theta_0 = 45°$. We propose that this is the reason why the initial elastic modulus shown in Figure 4 has a minimum for $\theta_i = 45°$. Moreover, if we could decouple the spontaneous and elastic strains, we would likely be able to calculate initial elastic modulus values that would better agree with those predicted by eq 3 and classical elastic theory.

The Director–Moduli Relationship

By linking together the results of the previous two sections, we are able to deduce relationships between the strain-dependent director angle and the nonlinear load curves. Rearranging eq 3 to give the deformation, λ_x, as a function of current and initial director angles (θ and θ_i, respectively—see Supporting Information Section 2) and inserting this into eq 2, we can plot the elastic modulus against director angle for each experiment (Fig. 6).

The most striking feature of Figure 6 is that for the range of director angles between ~15° and ~70°, the plotted curves
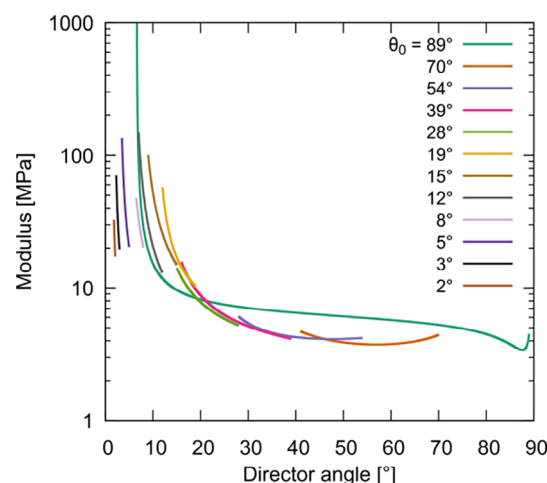

FIGURE 6 Using the inverse sigmoidal functions (eq 2) fitted to the tensile load curves and the Bladon model for director rotation with strain (eq 5), we can produce plots, for each experiment, of the elastic modulus against director angle θ. For the range of $15° < \theta < 70°$, the curves significantly overlap suggesting that deformation behavior in this range is independent of strain and the LCE deforms with a constant LC order parameter. [Color figure can be viewed at wileyonlinelibrary.com]

largely overlap with one another. This means that over this range of director angles, the elastic modulus of the LCE is predominantly dependent on the current director angle present and that strain dependencies are a secondary contribution. In turn, this implies that, in the region of overlapping curves, imposed stresses only cause the polymer conformation to rotate without being deformed (which would affect the elastic modulus preventing the curves overlapping). Moreover, as the polymer conformation shape and tensoral LC order parameter are intrinsically linked, we can conclude that the LC order parameter remains largely constant for deformations within this region of director angles.

By comparison, for initial director angles less than ~15°, the director rotates by much smaller amounts and the curves no longer overlap with one another. In this region, it is therefore likely that the deformation of the polymer conformation dominates the nonlinear mechanical behavior observed. The shape of the 88° curve is more difficult to interpret as the majority of the plateau-like region of the curve corresponds to a relatively small change in strain and so much of the behavior is confined to extremes of the curve.

Master Curves, Empirical Equations, and Modeled Deformations

Figure 6 tells us that in the region of $15° < \theta < 70°$, the tensile load curves plotted in Figure 3 will have equal moduli (i.e., equal gradients) at points of corresponding director angle. It is therefore reasonable to expect that the curves could form a master curve if they are superpositioned via points of equal director orientation. Such a master load curve for generic uniaxial deformations would allow for generalized

TABLE 2 Shift Factors Used to Translate the Individual Director–Strain and True Stress Load Curves to Form Their Respective Master Curves Shown in Figures 7(a) and 8

Sample θ_i (°)	Individual Strain Shift Factor	Cumulative Strain Shift Factor	Individual Stress Shift Factor (MPa)	Cumulative Stress Shift Factor (MPa)
70	0	0	0	0
54	0.56	0.56	2.26	2.26
39	0.52	1.08	2.37	4.63
28	0.28	1.36	1.42	6.06
19	0.49	1.85	4.36	10.42

predictions of the LCE uniaxial mechanical behavior (for the range of $15° < \theta < 70°$) predicted solely from the initial director angle and the applied stress.

In order to form the superpositioned master load curve, we must first identify the stresses and strains by which the individual load curves must be shifted. We first identify the strain shift factors required to form a director rotation–strain master curve using the data of Figure 5. Although we showed in Figure 5 that the (complicated) Bladon model well describes the director rotation behavior for the LCE, we here use (simpler) linear curves—fitted to each data set from Figure 5. Between curves of adjacent θ_i, there are a range of overlapping director angles, all of which could have been used for creating our superposition. We chose to use the midpoint of overlapping angles. To illustrate the process, we discuss the strain shift factor of the $\theta_i = 39°$ data relative to the $\theta_i = 54°$ data.

From the last recorded angle of the 54° curve (30.9°) and the first recorded angle of the 38° curve (which by definition is 38°), we calculate the average angle (34.5°). Using the fitted linear curves, we can calculate strains of the $\theta_i = 54°$ and 39° curves for $\theta = 34.5°$. The difference between these strains gives a

strain of 0.52 (Table 2), which corresponds to the strain the 39° director orientation and load curve data needed to be shifted by along the strain axis in order to superpose with the 54° curve. As the 54° will itself need to be shifted by a strain, calculated as 0.56 (Table 2), in order to superpose onto the 70° curve, the 39° curve would need to be shifted by the cumulative strain shift factor of (0.52 + 0.56 = 1.08). The second and third columns of Table 2 give the individual and cumulative strain shift factors calculated for each set of director orientation–strain data (Fig. 5) and stress–strain data (Fig. 3).

Figure 7(a,b) shows the strain-shifted director orientation–strain and stress–strain curves of Figures 5 and 3, respectively. The transposition of the director orientation data has led to the data collapsing onto a master director (MD) curve, which has been fitted to a linear curve of the form

$$\theta = 68.5 - 27.6 \times \epsilon. \tag{7}$$

The shifted stress–strain curves of Figure 7(b) do not yet form a master curve; however, they have been shifted to positions such that where they overlap they are expected (from Fig. 4) to have the same moduli (gradients).
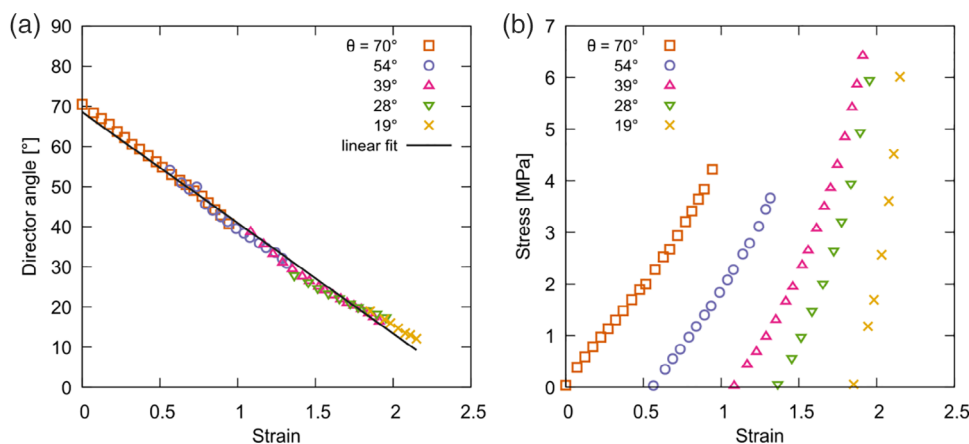

FIGURE 7 (a) MD curve formed by shifting individual director–strain curves to overlap with one another. (b) The corresponding true stress load curves shifted by the same amounts to positions where they are expected to have matching gradients (elastic moduli). [Color figure can be viewed at wileyonlinelibrary.com]

Repeating a similar process as above for the $\theta_i = 19°$ to $70°$ stress–strain data, but now using the fitted inverse sigmoidal function (eq 1) and fitted parameters from Table 1, we calculated the individual and cumulative stress shift factors, shown in the fourth and fifth columns of Table 2, respectively. Figure 8 plots the strain and stress-shifted $\theta_i = 19 – 70°$ load curves of Figure 3 and shows that as predicted from the result of Figure 4, the gradients between the overlapping portions of the stress–strain curves match exceptionally well with one another. The result is that the curves collapse onto a single seamless director–modulus superposition (DMS) curve that can be well fitted by an inverse sigmoidal function of

$$\sigma = 4.39 \times \log\left(\frac{1 + 0.426\epsilon}{1 - 0.444\epsilon}\right). \tag{8}$$

An Empirical Model

Given that we, for our LCE, were able to create two continuous curves linking the evolution of the director orientation and the stress to imposed strains, we can now develop an empirical model describing the behavior of the LCE in response to arbitrary uniaxial stresses applied at angles in the range of $15° < \theta < 70°$ to the LC director.

For clarity, we proceed with the forms of the DMS and MD curves (eqs 8 and 7, respectively) with the numerical constants replaced by symbols:

$$\sigma = A \times \log\left(\frac{1 + c\epsilon}{1 - d\epsilon}\right), \tag{9a}$$

$$\theta = \alpha - \beta\epsilon. \tag{9b}$$

By specifying a particular initial director angle, θ_i, between $15°$ and $70°$, at which a stress is applied, we can rearrange eq

18
16
14
12
10
8
6
4
2
0

True Stress [MPa]

0   0.5   1   1.5   2   2.5
Strain

$\theta = 70°$ □
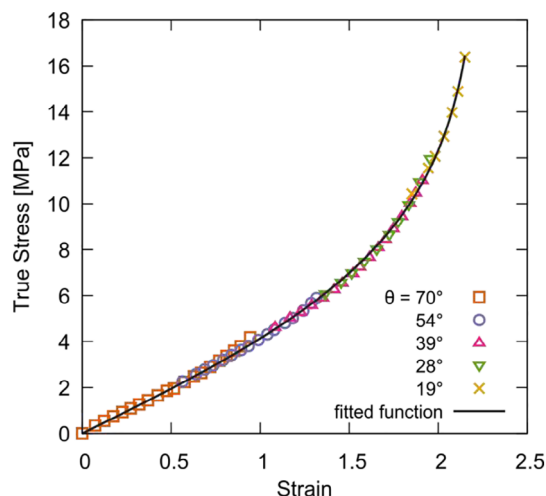54° ○
39° △
28° ▽
19° ✕
fitted function ——

FIGURE 8 Master curve from which generic deformations of LCE *A* with director angles between $15°$ and $70°$ can be deduced. [Color figure can be viewed at wileyonlinelibrary.com]

8b to identify the starting strain, ϵ_i, of the DMS and MD curves.

$$\epsilon_i = \frac{\alpha - \theta_i}{\beta}. \tag{10}$$

Feeding ϵ_i into eq 8a provides the zero-stress level, σ_i, from the DMS curve. If the origin were now shifted to (ϵ_i, σ_i) on the DMS curve, the resultant curve (in the positive quadrant) would correspond to the expected true stress load curve for the LCE stressed at θ_i to the LC director.

If this hypothetical sample were strained by $\Delta\epsilon$, the final strain, ϵ_f, according to the DMS and MD curves would be

$$\epsilon_f = \epsilon_i + \Delta\epsilon, \tag{11}$$

which would correspond to a DMS curve final stress level of

$$\sigma_f = A \times \log\left(\frac{1 + c(\epsilon_i + \Delta\epsilon)}{1 - d(\epsilon_i + \Delta\epsilon)}\right). \tag{12}$$

Therefore, the true stress, $\sum_T$, induced within the sample is given by

$$\sum_T = \sigma_f - \sigma_i, \tag{13a}$$

$$\sum_T = A \times \log\left(\frac{1 + c(\epsilon_i + \Delta\epsilon)}{1 - d(\epsilon_i + \Delta\epsilon)} \times \frac{1 - d\epsilon_i}{1 + c\epsilon_i}\right), \tag{13b}$$

and so the engineering stress, $\sum_E$, is given by

$$\sum_E = \frac{1}{1 + \Delta\epsilon}\left[A \times \log\left(\frac{1 + c(\epsilon_i + \Delta\epsilon)}{1 - d(\epsilon_i + \Delta\epsilon)} \times \frac{1 - d\epsilon_i)}{1 + c\epsilon_i}\right)\right]. \tag{14}$$

Given the linear relationship of the MD curve in Figure 7(a), we can also find the expected magnitude of director rotation, $\Delta\theta$, from the imposed strain, $\Delta\epsilon$,

$$\Delta\theta = \beta \times \Delta\epsilon. \tag{15}$$

The ease with which the above relationships have been derived is attributed to the simple forms of the MD and DMS curves (eq 9a,9b) which are readily inverted.

Testing the Model

Figure 9(a) plots the engineering load curves from the samples tested with θ_i between $19°$ and $70°$ along with model load curves using eq 14 and the same values of θ_i. The curves generated from the empirical model demonstrate a remarkable level of agreement with the experimental data, verifying the accuracy of the empirical model. Given this level of agreement, we propose that empirical models of LCE deformations have significant potential for predicting the
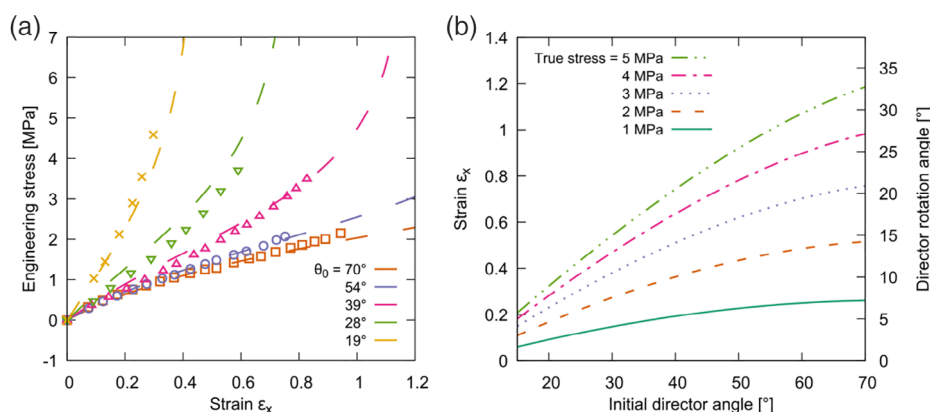
FIGURE 9 (a) Verification of the accuracy of the model developed by regenerating load curves for the original mechanical responses and comparing them to the experimentally measured data. (b) Alternative representation of the empirical model that would be useful for predicting deformations and the director response based on applied true stresses and initial director angles. [Color figure can be viewed at wileyonlinelibrary.com]

deformation behavior for LCEs with complex director geometries.

Inverting eq 13b to give the strain, $\Delta\epsilon$, as a function of true stress, $\sum_T$, and ϵ_i (and hence θ_i via eq 13a) yields

$$\Delta\epsilon = \frac{(1+c\epsilon_i)(1-d\epsilon_i)\left(1+\exp\left(\sum_T/A\right)\right)}{c(1-d\epsilon_i)+d(1+c\epsilon_i)\exp\sum_T/A}, \quad (16)$$

Figure 9(b) plots eq 16 to show the expected strain, $\Delta\epsilon$, as a function of initial director angle, θ_i, for a several different applied true stresses. This alternative representation of the deformation behavior of the LCE would be useful in device design if the target true stress for a system is known and a target strain is required. The optimal initial director angle can then be found by generating the relevant curve. Moreover, as eq 15 shows the director rotation is proportional to the strain of the sample, the final director angle can also easily be extracted from Figure 9(b) via the right hand axes. As one would have expected, Figure 9(b) shows that larger strains can be obtained by applying larger stresses and by increasing the initial angle between the director and the stress axis.

The presented form of the model is, however, not without limitations. If one aims to design a device based on a stress which can be applied, then it will be the engineering stress that would be known as opposed to the true stress. Equivalent versions of the equations used to generate Figure 9(b) cannot be derived analytically as this would require inverting eq 14 to have the strain, $\Delta\epsilon$, as a function of the engineering stress, $\sum_E$, and θ_i. To generate such curves, numerical methods to invert eq 14 would be required.

Extending the Model to Geometry Changes
By applying a similar process as above, we can also attempt to develop an empirical model to describe the geometrical

deformations of the LCE when strained at angles between $15°$ and $70°$.

Figure 10 plots the transverse strains along y and z axes for tested samples with initial director angles $\geq 19°$. Data for samples $\leq 19°$ have, for clarity, not been plotted here; however, they are shown in Supporting Information Figure S3. Each data set of Figure 10 shows anisotropy between the strain responses in the y and z transverse directions. While the strains along y are largely linear, the strains along z are highly nonlinear—that is, the instantaneous Poisson's ratio ν_{xz} varies with strain ϵ_x. The $88°$ sample shows a minimum in ϵ_z ($\nu_{xz} = 0$), beyond which the material enters a negative Poisson's ratio (or auxetic) regime—a phenomena previously discussed.[16] The $39°$, $54°$, and $70°$ curves show similar behavior as they tend to a plateau in ϵ_z. Given this shared feature of ϵ_z, it seems plausible that these samples may have also entered an auxetic regime if they had not failed when they did.

To a first approximation, the transverse strains, ϵ_y, of the $15°$–$70°$ samples show identical linear behavior. Fitting a linear curve to these data, constrained to pass through the origin, yields

$$\epsilon_y = -0.35 \times \epsilon_x. \quad (17)$$

By replacing ϵ_x for $\Delta\epsilon$ (deduced in eq 17) from equation, we can attempt to predict the transverse strain along y in response to an applied true stress. Further by using the fact that the present LCE is known to deform at constant volume (i.e., $\lambda_x\lambda_y\lambda_z = 1$), we can extract model predictions for the transverse deformations along z as a function of applied true stress.[16]

For the experimentally measured cases of $\theta_i = 19° - 70°$, Figure 11 plots model transverse deformations as a function of applied true stress against the original data. While the predictions of Figure 11 are comparatively worse than the level
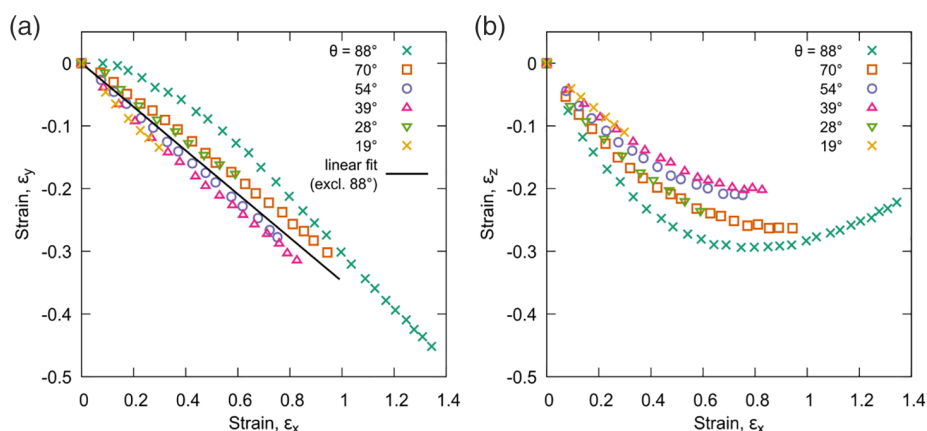
FULL PAPER

WWW.POLYMERPHYSICS.ORG

JOURNAL OF
POLYMER SCIENCE

Polymer
Physics

FIGURE 10 Transverse strains along the (a) y and (b) z axes for samples with initial angles, $\theta_i \geq 19°$, according to the coordinate system illustrated by Figure 1. Strains along the z axis are determined from strains measured in the xy plane and the constant volume condition. Transverse strains along y for the $19°$–$70°$ samples replotted from Figure 4 along with a fitted line which, to a first approximation, each of the curves follows. [Color figure can be viewed at wileyonlinelibrary.com]
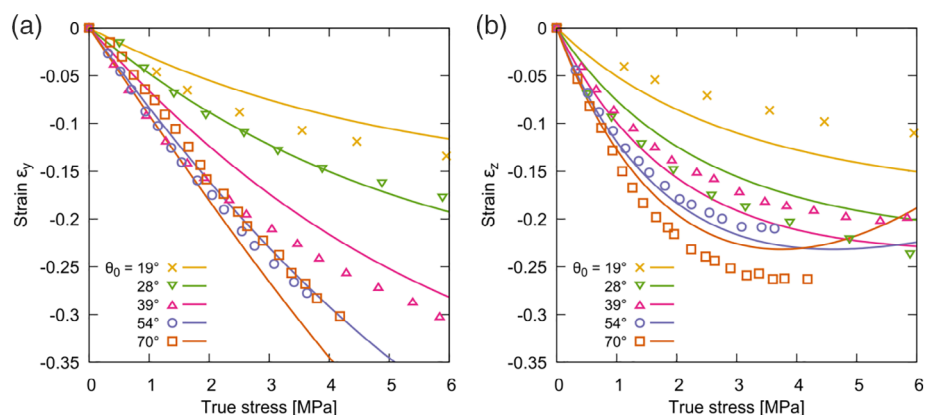

FIGURE 11 Predictions for the transverse strains along the (a) y and (b) z axes compared against experimentally measured strains. [Color figure can be viewed at wileyonlinelibrary.com]

of agreement between the model load curves of Figure 9(a), they still offer a reasonably good model, which could still be useful for a first prediction of the complete geometry changes of LCE under deformation.

Interestingly, the curves shown in Figure 11(b) suggest the emergence of auxetic behavior for the $54°$ and $70°$ curves. These results suggest that the auxetic response of the LCE may be tuned via θ_i in addition to tuning via polymer conformation anisotropy as previously suggested. Theoretically, the predictions of auxeticity by Warner and Terentjev apply only to stresses applied perpendicular to director—stresses at other angles remain uninvestigated.[32]

CONCLUSIONS

In this study, we have reported, for the first time, experimental results for the tensile load and director rotation behavior of an LCE stressed at a variety of different angles relative to the LC director. We have seen that the material displays

highly nonlinear behavior, which is also anisotropic. While the anisotropy in elastic moduli broadly agrees with expectations for uniaxial anisotropic materials, the additional complexities reported show the mechanical richness of LCEs continues to grow.

Given the anisotropic nature of many biological tissues, we believe the controllable anisotropic deformations of LCEs demonstrated here could have applications to biomimetic soft robotic and biomedical devices. While LCEs have been touted for such applications in the past, one of the limitations has been an unknown theoretical relationship between director angle, director rotation, and tensile load behavior. In this work, we have shown that empirical methods can accurately describe much of the uniaxial tensile behavior of LCEs. While the mechanical behaviors of LCEs also depend on their particular chemistries, we believe the accuracy of the empirical model derived here, and the ease with which it was created, shows the promise of such techniques for modeling the behavior of LCEs and designing LCE-based mechanical devices. The

need for such models is becoming increasingly important as LCEs are stepping ever closer to commercial application and so will need to be rigorously modeled and tested—something not yet possible using purely theoretical models.

A particularly striking result of this paper is how well the inverse sigmoidal function fitted to all of the load curves presented. While it is always possible to fit any function to a data set given enough free parameters, the function chosen only had three free parameters and fits extremely well to all 12 data sets. We noted that there was no known theoretical basis for our choice of function. However, given the quality of the fits, we propose the fits and data shown could guide the further development of theory to build our fundamental understanding of the mechanical behaviors of this remarkable class of materials.

ACKNOWLEDGMENTS

REFERENCES AND NOTES

1 A. Jaggessar, H. Shahali, A. Mathew, P. K. D. V. Yarlagadda, *J. Nanobiotechnology* **2017**, *15*, 64.

2 O. Okay, *J. Mater. Chem. B* **2019**, *7*, 1581.

3 P. Egan, R. Sinko, P. R. Leduc, S. Keten, *Nat. Commun.* **2015**, *6*, 7418.

4 S. Schuhladen, F. Preller, R. Rix, S. Petsch, R. Zentel, H. Zappe, *Adv. Mater.* **2014**, *26*, 7247.

5 S. Coyle, C. Majidi, P. LeDuc, K. J. Hsia, *Extrem. Mech. Lett.* **2018**, *22*, 51.

6 L. Montero de Espinosa, W. Meesorn, D. Moatsou, C. Weder, *Chem. Rev.* **2017**, *117*, 12851.

7 L. E. Millon, M.-P. Nieh, J. L. Hutter, W. Wan, *Macromolecules* **2007**, *40*, 3655.

8 F. Ilievski, A. D. Mazzeo, R. F. Shepherd, X. Chen, G. M. Whitesides, *Angew. Chem. Int. Ed.* **2011**, *50*, 1890.

9 R. L. Truby, J. A. Lewis, *Nature* **2016**, *540*, 371.

10 P. D. Olmsted, *J. Phys. II* **1994**, *4*, 2215.

11 H. Zeng, P. Wasylczyk, C. Parmeggiani, D. Martella, M. Burresi, D. S. Wiersma, *Adv. Mater.* **2015**, *27*, 3883.

12 J. M. Boothby, H. Kim, T. H. Ware, *Sens. Actuators B* **2017**, *240*, 511.

13 T. Guin, M. J. Settle, B. A. Kowalski, A. D. Auguste, R. V. Beblo, G. W. Reich, T. J. White, *Nat. Commun.* **2018**, *9*, 1.

14 P. Bladon, E. M. Terentjev, M. Warner, *Phys. Rev. E* **1993**, *47*, R3838.

15 H. Higaki, T. Takigawa, K. Urayama, *Macromolecules* **2013**, *46*, 5223.

16 D. Mistry, S. D. Connell, S. L. Mickthwaite, P. B. Morgan, J. H. Clamp, H. F. Gleeson, *Nat. Commun.* **2018**, *9*, 5095.

17 H. Wermter, H. Finkelmann, *e-Polymers* **2001**, *1*, 111.

18 H. Finkelmann, E. Nishikawa, G. G. Pereira, M. Warner, *Phys. Rev. Lett.* **2001**, *87*, 015501.

19 D. Mistry, P. B. Morgan, J. H. Clamp, H. F. Gleeson, *Soft Matter* **2018**, *14*, 1301.

20 T. J. White, D. J. Broer, *Nat. Mater.* **2015**, *14*, 1087.

21 L. T. de Haan, C. Sánchez-Somolinos, C. M. W. Bastiaansen, A. P. H. J. Schenning, D. J. Broer, *Angew. Chem. Int. Ed.* **2012**, *51*, 12469.

22 T. H. Ware, J. S. Biggins, A. F. Shick, M. Warner, T. J. White, *Nat. Commun.* **2016**, *7*, 10781.

23 R. Rihani, H. Kim, B. Black, R. Atmaramani, M. Saed, J. Pancrazio, T. Ware, *Micromachines* **2018**, *9*, 416.

24 M. O. Saed, R. H. Volpe, N. A. Traugutt, R. Visvanathan, N. A. Clark, C. M. Yakacki, *Soft Matter* **2017**, *13*, 7537.

25 Y. Gao, T. Mori, S. Manning, Y. Zhao, A. D. Nielsen, A. Neshat, A. Sharma, C. J. Mahnen, H. R. Everson, S. Crotty, R. J. Clements, C. Malcuit, E. Hegmann, *ACS Macro Lett.* **2016**, *5*, 4.

26 I. Kundler, H. Finkelmann, *Macromol. Rapid Commun.* **1995**, *16*, 679.

27 H. Hirschmann, P. M. S. Roberts, F. J. Davis, W. Guo, C. D. Hasson, G. R. Mitchell, *Polymer (Guildf).* **2001**, *42*, 7063.

28 I. Kundler, H. Finkelmann, *Macromol. Chem. Phys.* **1998**, *199*, 677.

29 G. Mitchell, F. Davis, W. Guo, *Phys. Rev. Lett.* **1993**, *71*, 2947.

30 R. V. Talroze, E. R. Zubarev, S. A. Kuptsov, A. S. Merekalov, T. I. Yuranova, N. A. Plate', H. Finkelmann, *React. Funct. Polym.* **1999**, *41*, 1.

31 D. Allan, T. Caswell, N. Keim, C. Van Der Wel, trackpy: Trackpy v0.3.2. Zenodo. http://doi.org/10.5281/zenodo.60550 **2016**.

32 M. Warner, E. M. Terentjev, *Liquid Crystal Elastomers*; Clarendon Press: Oxford, **2013**.

33 J. C. Gerdeen, R. A. L. Rorrer, *Engineering Design with Polymers and Composites*, 2nd ed.; CRC Press: Boca Raton, **2011**.

34 S. Gantenbein, K. Masania, W. Woigk, J. P. W. Sesseg, T. A. Tervoort, A. R. Studart, *Nature* **2018**, *561*, 226.

35 G. R. Mitchell, F. J. Davis, W. Guo, R. Cywinski, *Polymer (Guildf)*, **1991**, *32*, 1347.

36 P. Bladon, E. Terentjev, M. Warner, *J. Phys. II Fr.* **1994**, *4*, 75.